How uniform is the peptide plane geometry? A high-accuracy NMR study of dipolar Cα–C′/HN–N cross-correlated relaxation

ARTICLE *in* JOURNAL OF BIOMOLECULAR NMR · JUNE 2011

Impact Factor: 3.14 · DOI: 10.1007/s10858-011-9519-z · Source: PubMed

1 AUTHOR:

Beat Vögeli
ETH Zurich
46 PUBLICATIONS **813** CITATIONS

SEE PROFILE

J Biomol NMR (2011) 50:315–329
DOI 10.1007/s10858-011-9519-z

ARTICLE

How uniform is the peptide plane geometry? A high-accuracy NMR study of dipolar C^{α}–C'/H^{N}–N cross-correlated relaxation

Beat Vögeli

Received: 27 April 2011 / Accepted: 17 May 2011 / Published online: 3 June 2011

Abstract Highly precise and accurate measurements of very small NMR cross-correlated relaxation rates, namely those between protein H_i^N–N_i and C_{i-1}^{α}–C_{i-1}' dipoles, are demonstrated with an error of 0.03 s^{-1} for GB3. Because the projection angles between the two dipole vectors are very close to the magic angle the rates range only from -0.2 to $+0.2$ s^{-1}. Small changes of the average vector orientations have a dramatic impact on the relative values. The rates suggest deviation from idealized peptide plane geometry caused by twists around the C′–N bonds and/or pyramidalization of the nitrogen atoms. A clear alternating pattern along the sequence is observed in β strands 1, 3 and 4 of GB3, where the side chains of almost all residues with large positive rates are solvent exposed. In the α helix all rates are relatively large and positive. Some of the currently most accurate structures of GB3 determined by both high resolution X-ray crystallography and NMR are in satisfactory agreement with the experimental rates in the helix and β strand 3, but not in the loops and the two central strands of the sheet for which no alternating pattern is predicted.

Keywords Cross-correlated relaxation · GB3 · Peptide plane · ω angle

Electronic supplementary material The online version of this article (doi:10.1007/s10858-011-9519-z) contains supplementary material, which is available to authorized users.

B. Vögeli (✉)
Laboratory of Physical Chemistry, Swiss Federal Institute of Technology, ETH-Hönggerberg, 8093 Zürich, Switzerland
e-mail: beat.voegeli@phys.chem.ethz.ch

Introduction

An atom-resolved picture of the structure and dynamics of biomolecules is a key prerequisite not only for understanding protein activities such as molecular recognition, enzymatic activity, folding, *et cetera*, but also for validation of quantum chemical calculations or calibration of force field parameters (Fersht 1998; Whitford 2005; Branden and Tooze 1999). Most structural modeling routines assemble 3D protein backbones by linking uniform peptide planes under the sole variation of the φ and ψ dihedral angles or allow for minimal additional degrees of freedom (for example, the ω angle in X-ray crystallography) (Wüthrich 1986; Brunger 1993; Koradi et al. 1996; MacArthur and Thornton 1996; Güntert et al. 1997; Schwieters et al. 2003; Bradley et al. 2005; Schwieters et al. 2006). The peptide plane is constituted by the heavy-atom chain C_{i-1}^{α}–N_i–C_i'–C_i^{α}. O_i and H_i^N are usually placed in the plane near or at idealized angles (Pauling et al. 1951; Corey and Pauling 1953; Eisenberg 2003). Several publications, however, have challenged this uniformity by suggesting twists around C′–N bonds and pyramidalization of the nitrogen atoms (Pauling and Corey 1951; Winkler and Dunitz 1971; Dunitz and Winkler 1975; MacArthur and Thornton 1996; Head-Gordon et al. 1991; Engh and Huber 1991; Edison et al. 1994; Sulzbach et al. 1995; Hu and Bax 1997).

Recent studies have been motivated by the introduction of the residual dipolar coupling (RDC) methodology in NMR spectroscopy (Tjandra and Bax 1997; Tolman et al. 2001). RDCs depend on the bond orientation in a molecule-fixed frame in a very sensitive manner, and thus are ideal for addressing the issue. Ulmer et al. used large sets of RDCs to refine a high-resolution crystal structure of the protein GB3 (Gronenborn et al. 1991; Derrick and Wigley

1994) to demonstrate a considerable deviation from ideal geometry (Ulmer et al. 2003). In particular, they concluded that the H^N–N bond deviates by up to $\approx 5°$ in-plane and $\approx 10°$ out-of-plane from the vector bisecting the C′–N–C^α angle. Highly precise H^N–H^α *J*-couplings and intraresidual and sequential H^N–H^α RDCs have been shown to be in better agreement with this refined geometry (Vögeli et al. 2007, 2008). Recently, H^N–N, H^α–C^α and C^α–C′ RDCs obtained under 6 alignment conditions have been used to determine bond orientations simultaneously with order parameters at very high accuracy and precision (Yao et al. 2008a, b). Root-mean-square deviations of the H^N–N and H^α–C^α bonds were calculated to be 5.2° and 3.6° from ideal orientation.

To improve the characterization of the peptide plane geometry it is desirable to obtain direct restraints between these individual bonds. NMR cross-correlated relaxation (CCR) rates depend on the relative orientation of two tensorial interactions (Goldman 1984; Daragan and Mayo 1997; Kumar et al. 2000). It has been recognized that CCR rates also report on dynamics on all time scales (Pelupessy et al. 2003; Vugmeyster et al. 2004; Vögeli 2010). Since the initial proposal to use CCR rates for determination of backbone torsion angles (Reif et al. 1997), a wealth of experiments has been designed to measure CCR rates depending on the ω angle and peptide plane fluctuations. Sums of H_i^N–N_i dipole/C_{i-1}' CSA and H_i^N–C_{i-1}' dipole/N_i CSA CCR rates have been measured and dynamics effects predicted on the basis of the 3D GAF model (Brutscher et al. 1998; Bremi et al. 1997; Bremi and Brüschweiler 1997). These rates have been remeasured and combined with sums of H_i^N–N_i dipole/C_{i-1}^α–C_{i-1}' dipole and H_i^N–C_{i-1}' dipole/C_{i-1}^α–N_i dipole CCR rates and sums of C_{i-1}^α–N_i dipole/N_i CSA and C_{i-1}^α–C_{i-1}' dipole/C_{i-1}' CSA CCR rates for determination of the peptide plane fluctuation using the 3D GAF model (Carlomagno et al. 2000). Deviation from rate uniformity was interpreted in terms of anisotropic peptide plane motion. H_i^N–C_{i-1}' dipole/C_{i-1}' CSA CCR rates have been interpreted with the 1D GAF model for peptide plane fluctuation (Früh et al. 2002) and simultaneous fits to H_i^N–N_i dipole/H_i^N–C_{i-1}' dipole, H_i^N–N_i dipole/H_i^N–C_i^α dipole and H_i^N–N_i dipole/N_i–C_{i-1}' dipole with 3D GAF (Bytchenkoff et al. 2005). Generally, the use of the CSA tensors complicates the analysis considerably because it is associated with uncertainties regarding the tensor elements as well as their orientation. More commonly, CCR rates with an intervening ω angle were used to determine other angles which are subjected to stronger fluctuations by assuming idealized geometry for the ω angle. Among these are ψ angles assessments by H_{i-1}^α–C_{i-1}^α dipole/H_i^N–N_i dipole (Reif et al. 1997; Yang and Kay 1998; Pelupessy et al. 1999a, b; Chiarparin et al. 1999; Reif et al. 2000; Kloiber et al. 2002; Vögeli and Pervushin 2002; Takahashi and Shimada 2007), H_i^α–C_i^α dipole/C_i' CSA (Yang and Kay 1998; Chiarparin et al. 1999; Takahashi and Shimada 2007; Yang et al. 1997, 1998; Sprangers et al. 2000), or joint (ψ,φ) angles by C_{i-1}' CSA/C_i' CSA (Skrynnikov et al. 2000) and by H_{i-1}^N–N_{i-1} dipole/H_i^N–N_i dipole (Pelupessy et al. 2003). Generally, the question arises as to how far an interpretation of motion can be taken without taking into consideration non-ideal geometry and anisotropic molecular tumbling (Vögeli 2010). It has been shown, for example, that a detailed interpretation of H_{i-1}^α–C_{i-1}^α dipole/H_i^N–N_i dipole CCR rates in GB3 requires exact knowledge of the diffusion tensor (Vögeli and Yao 2009).

In this study, it is demonstrated that very small CCR rates, namely those between H_i^N–N_i and C_{i-1}^α–C_{i-1}' dipoles, can be measured at very high precision and accuracy. The measurements are by almost one order of magnitude more precise than those presented in a previous work (Carlomagno et al. 2000). This reduction in combination with exact knowledge of molecular tumbling (diffusion tensor) and highly precise structures is critical for a detailed interpretation. Although the theoretically possible rate amplitude can be rather large the observed rate is small. Because the projection angle between the two dipole vectors is very close to the magic angle it ranges from -0.2 to $+0.2\ s^{-1}$ in small proteins. This condition bears very interesting effects: Small changes of the average vector orientation have a dramatic impact on the relative value of the rate. Therefore, these rates may be better structural probes than small rates for which the coupling strength is small (but the projection angle possibly very different from the magic angle). On the other hand, effects from dynamics are even smaller and escape interpretation at the current level of accuracy and precision. It is shown that the experimental range of values can be largely explained by the non-idealized geometry and anisotropic molecular tumbling. Although some of the most accurate structures currently available are used to evaluate the CCR rates measured on GB3 none of these is in good agreement.

Theory

Evolution of multiple quantum coherence, MQ, between spins I^1 and I^2, where I^1 is weakly scalar coupled to the passive spin S^1 (J_{I1S1}) and I^2 to S^2 (J_{I2S2}), yields four spectral peaks corresponding to the spin states of S^1 and S^2 ($\alpha\alpha$, $\alpha\beta$, $\beta\alpha$, and $\beta\beta$) for each coherence order (zero and double quantum coherence, ZQ and DQ). In the secular approximation, the I^1–S^1 dipole/I^2–S^2 dipole CCR rate, $R_{d(I1S1)/d(I2S2)}$, can be extracted together with $R_{d(I1S2)/d(I2S1)}$

from the peak intensities I of the components of the ZQ and DQ quadruplets:

$$\frac{1}{8T_{\mathrm{MQ}}}\ln\left(\frac{I^{\mathrm{ZQ}}_{\alpha\alpha}I^{\mathrm{ZQ}}_{\beta\beta}}{I^{\mathrm{ZQ}}_{\alpha\beta}I^{\mathrm{ZQ}}_{\beta\alpha}}\frac{I^{\mathrm{DQ}}_{\alpha\beta}I^{\mathrm{DQ}}_{\beta\alpha}}{I^{\mathrm{DQ}}_{\alpha\alpha}I^{\mathrm{DQ}}_{\beta\beta}}\right) = R_{\mathrm{d(I1S1)/d(I2S2)}} + R_{\mathrm{d(I1S2)/d(I2S1)}} \quad (1)$$

T_{MQ} is the constant time during which the coherences evolve. Note that in equation 1.3 in reference (Vögeli and Yao 2009) a negative sign is missing on one side. The same formal effect can be achieved by mixing the ZQ and DQ experimentally during T_{MQ} (Yang and Kay 1998). In that case, the ZQ and DQ quadruplets are superimposed yielding only one apparent quadruplet. The CCR rates are then obtained as

$$\frac{1}{4T_{\mathrm{MQ}}}\ln\left(\frac{I^{\mathrm{ZQ,DQ}}_{\alpha\alpha,\alpha\beta}I^{\mathrm{ZQ,DQ}}_{\beta\beta,\beta\alpha}}{I^{\mathrm{ZQ,DQ}}_{\alpha\beta,\alpha\alpha}I^{\mathrm{ZQ,DQ}}_{\beta\alpha,\beta\beta}}\right) = R_{\mathrm{d(I1S1)/d(I2S2)}} + R_{\mathrm{d(I1S2)/d(I2S1)}} \quad (2)$$

Under the assumption that radial and spherical motion of the i-j vectors is not correlated, the CCR rates can be expressed with effective distances $r^{\mathrm{eff}}_{\mathrm{ij}}$ between the nuclei i and j (Case 1999):

$$R_{\mathrm{d(I1S1)/d(I2S2)}} = \left(\frac{\mu_0}{4\pi}\right)^2\frac{\gamma_{\mathrm{I1}}\gamma_{\mathrm{S1}}\gamma_{\mathrm{I2}}\gamma_{\mathrm{S2}}\mathrm{h}^2}{10\pi^2}\frac{1}{\left(r^{\mathrm{eff}}_{\mathrm{I1S1}}\right)^3\left(r^{\mathrm{eff}}_{\mathrm{I2S2}}\right)^3} \times J_{\mathrm{d(I1S1)/d(I2S2)}}(0) \quad (3)$$

γ_{i} is the gyromagnetic ratio of nucleus i, μ_0 is the permeability of free space, h denotes Planck's constant, and $J_{\mathrm{d(A)/d(B)}}(0)$ the spectral density function at zero frequency associated with the interference between the dipolar interactions A and B. $R_{\mathrm{d(I1S2)/d(I2S1)}}$ is obtained by interchanging S^1 and S^2.

A simple model has been proposed to compare experimental to predicted CCR rates (Vögeli 2010). This model (1) incorporates fast (faster than molecular tumbling) and slow (slower than molecular tumbling) motion, (2) distinguishes between correlated and uncorrelated slow motion, and (3) is sensitive to the anisotropy of the molecular tumbling. It has been demonstrated that effects of anisotropy must be included in order to analyze orientation and fluctuation of the involved interactions (Vögeli and Yao 2009; Deschamps and Bodenhausen 2001). If the internal motions are separated from the molecular tumbling time by at least one order of magnitude, and no slow correlated motion between A and B is present the spectral density function can be approximated by assuming axially symmetric motion of A and B and the following expression is obtained:

$$J_{\mathrm{d(I1S1)/d(I2S2)}}(0) = S^{\mathrm{RDC}}_{\mathrm{I1S1}}S^{\mathrm{RDC}}_{\mathrm{I2S2}}J_{\mathrm{d(I1S1)/d(I2S2)}}(0)^{\mathrm{rigid}} \quad (4)$$

$S^{\mathrm{RDC}}_{\mathrm{ij}}$ is the order parameter obtained from the RDC between spins i and j. Note that other order parameters that are sensitive to slow timescales may be used instead. RDCs are sensitive to motions faster than milliseconds (Meiler et al. 2001; Peti et al. 2002; Tolman 2002). The spectral density of a hypothetically rigid molecule is

$$J_{\mathrm{d(I1S1)/d(I2S2)}}(0)^{\mathrm{rigid}} = \sum_{k=-2}^{2}\tau_k C^{\mathrm{int}}_k(\Omega_{\mathrm{I2S2}},\Omega_{\mathrm{I1S1}}) \quad (5)$$

$C^{\mathrm{int}}_k(\Omega_{\mathrm{I2S2}},\Omega_{\mathrm{I1S1}})$ are linear combinations of products of spherical harmonics and establish the angular dependence on the bond orientations. τ_{k} are inverse eigenvalues of the anisotropic diffusion operator (Favro 1960). They may be regarded as a generalized molecular tumbling time. Exact expressions can be looked up in reference (Vögeli 2010). In practice, it may be sufficient to assume the molecular tumbling to be axially symmetric. In that case, the expressions simplify considerably and the explicit expression is

$$\begin{aligned} J_{\mathrm{d(I1S1)/d(I2S2)}}(0)^{\mathrm{rigid,axial}} &= \tau_0\frac{1}{4}(3\cos^2\theta_{\mathrm{I1S1}}-1)(3\cos^2\theta_{\mathrm{I2S2}}-1) \\ &+ \tau_{\pm1}\frac{3}{4}\sin 2\theta_{\mathrm{I1S1}}\sin 2\theta_{\mathrm{I2S2}}\cos(\varphi_{\mathrm{I1S1}}-\varphi_{\mathrm{I2S2}}) \\ &+ \tau_{\pm2}\frac{3}{4}\sin^2\theta_{\mathrm{I1S1}}\sin^2\theta_{\mathrm{I2S2}}\cos(2\varphi_{\mathrm{I1S1}}-2\varphi_{\mathrm{I2S2}}) \end{aligned} \quad (6)$$

(θ_{ij}, φ_{ij}) are the polar angles of the i-j vector. Note that (4, 6) may not be satisfactory approximations when different rotamer states in side chains are involved (Carlomagno et al. 2003; Vögeli and Riek 2010).

Slow correlated motion, however, causes an inequality in (4). The right-hand side becomes larger than $J_{\mathrm{d(I1S1)/d(I2S2)}}(0)$ for correlated motion, and smaller for anticorrelated motion, respectively. If the deviation is larger than the experimental error and additional errors introduced by the model assumptions (Vögeli 2010) conclusions on the degree of correlation may be drawn.

In the current study on GB3, assumption of anisotropy in tumbling is indispensable. For uniform standard peptide bond geometry and isotropic tumbling, a unique CCR rate value of $\approx$0.058 s^{-1} is expected for all residues. However, the ratio of the main axis of the diffusion tensor to the averaged perpendicular axis is $\approx$1.4 and there is a small rhombic component (Hall and Fushman 2003). Pearson's correlation coefficient for correlation plots between CCR rates predicted with the isotropic and anisotropic model is 0.70 and 0.88, respectively, for 2OED with optimized proton position (Ulmer et al. 2003; Yao et al. 2008a, b) and for an ensemble (Clore and Schwieters 2006) (see also the plot in reference (Vögeli 2010)). This results for both structures in a pairwise rmsd of $\approx$0.05 s^{-1}.

In Fig. 1, $R = R_{\mathrm{HN/C\alpha C'}} + R_{\mathrm{HNC'/C\alpha N}}$ is simulated in dependence on the projection angles C^{α}–C′–N (arccosine

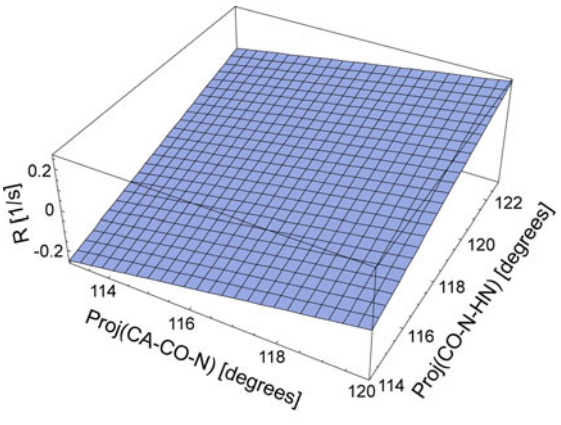

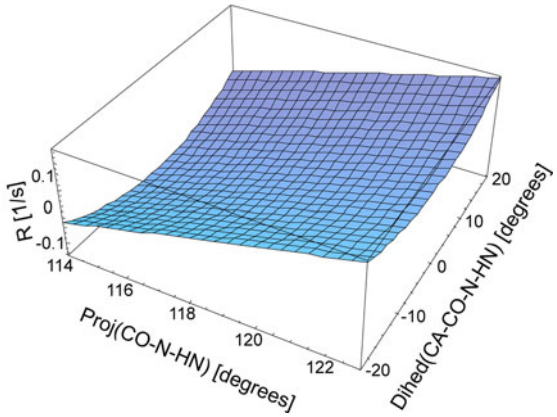

Fig. 1 Simulated CCR rate $R = R_{\mathrm{HN/C\alpha C'}} + R_{\mathrm{HNC'/C\alpha N}}$ in dependence on the projection angles C^{α}–C′–N and C′–N–H^{N} (*left*) and the projection angle C′–N–H^{N} and the dihedral angle C^{α}–C′–N–H^{N} (*right*). The chosen ranges reflect the distributions of the projection angles sampled by the 2OED and ensemble structures (Ulmer et al. 2003; Clore and Schwieters 2006) and the variations in the ω angle proposed in the literature (Head-Gordon et al. 1991; Engh and Huber 1991; Edison et al. 1994). Isotropic molecular tumbling is assumed

of the normalized scalar product between C^{α}–C′ and N–C′) and C′–N–H^{N}, and the dihedral angle C^{α}–C′–N–H^{N}. For simplicity, the molecular tumbling is assumed to be isotropic. As opposed to more commonly measured dipole/dipole CCR rates, the unwanted but inseparable contribution from the second term is relatively large and must be included in the analysis. On average, it is $\approx$20% of the wanted contribution but ranges from 5 to 450%. Interestingly, R is moderately sensitive to variations of the dihedral angle and thus also of the ω angle. On the other hand, the projection angles dominate the range of R with a near-linear dependence. Note that additional variation is caused by the tumbling anisotropy.

Experimental section

Sample expression and purification

GB3 was expressed and purified as described previously (Ulmer et al. 2003). The {^{2}H,^{13}C,^{15}N}-labeled NMR sample contained 500 µl of 2 mM protein solution in 95% H_2O, 5% D_2O, 50 mM potassium phosphate buffer, pH 6.5, and 0.5 mg/mL sodium azide.

NMR spectroscopy

The 3D ct-HNCO pulse sequences for the measurement of $R_{\mathrm{d(HNN)/d(C\alpha C')}} + R_{\mathrm{d(HNC')/d(C\alpha N)}}$ CCR rates are shown in Fig. 2. They are essentially constant-time modifications of the 3D HNCO initially designed for dipole/CSA CCR rate measurements associated with MQ[$^{15}N_i$,$^{13}C_{i-1}'$] (Brutscher et al. 1998). The first approach relies on the evolution of all multiplet components of the multiple quantum coherences in a four spin system. This approach is referred to as "all components evolution", or ACE. $^{1}H_i^{N}$ polarization is excited and converted into multiple quantum coherences MQ[$^{15}N_i$,$^{13}C_{i-1}'$] via $^{15}N_i$ in two INEPT steps. The MQ coherences are chemical-shift labeled under scalar coupling to $^{1}H_i^{N}$ and $^{13}C_{i-1}^{\alpha}$ during τ_{mix} yielding four components (doublets of doublets) for both the ZQ and the DQ coherences. Subsequently, the magnetization is converted into single-quantum $^{15}N_i$ for chemical-shift labeling and transferred back to $^{1}H_i^{N}$ for direct detection. Two subspectra, (ZQ-DQ) and (ZQ + DQ), are recorded, and subsequently added (subtracted) to obtain the ZQ (DQ) spectra. Experimental details are provided in Fig. 2. An upper limit to τ_{mix} is given by various small scalar couplings. The most important ones are $^{3}J_{\mathrm{C'(i-2),C'(i-1)}}$ and $^{3}J_{\mathrm{C'(i-1),C'(i)}}$ which can exceed 2 Hz. Using the Karplus parametrization proposed in (Hu and Bax 1996), peaks intensities may lose 80% under unfortunate φ_{i-1} and φ_i angles with $\tau_{\mathrm{mix}} = 140$ ms. Loss of more than 50% is predicted for residues 14–21, and 45 in GB3. In addition, scalar coupling to side-chain CO, namely $^{3}J_{\mathrm{C'(i-1),CO(i-1,SC)}}$ and $^{3}J_{\mathrm{N(i),CO(i,SC)}}$, in ASN and ASP, which may exceed 4 Hz and 2 Hz, respectively, may also cause significant signal loss. Here, residues 40, 41 and 46–48 lose more than 50% based on the Karplus parametrization proposed by (Perez et al. 2001). All other active couplings such as $^{2}J_{\mathrm{N(i-1),C'(i-1)}}$, $^{2}J_{\mathrm{N(i),C'(i)}}$, $^{3}J_{\mathrm{N(i-1),N(i)}}$ and $^{3}J_{\mathrm{N(i),N(i+1)}}$ and those across hydrogen bonds are smaller than 1 Hz and their impact is negligible.

It has been proposed to mix the ZQ and DQ coherences during the experiment (Skrynnikov et al. 2000) in order to increase the signal-to-noise ratio. This approach is referred to as "mixed multiple quantum", or MMQ. Application of any two inversion pulses simultaneously during τ_{mix} leaves the effective dipole/dipole relaxation superoperator involving all 4 spins unchanged. Simultaneous mixing of ZQ and DQ and chemical-shift labeling requires at least 3

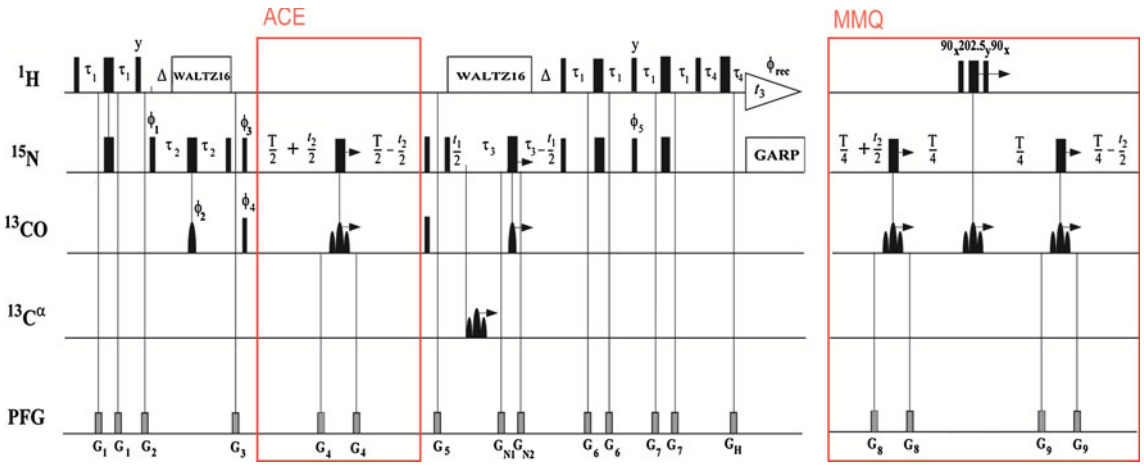

Fig. 2 Pulse sequences of the 3D ct-HNCO experiments for the measurement of $R = R_{HNN/C\alpha C'} + R_{HNC'/C\alpha N}$. The radio-frequency pulses on ^{1}H, ^{15}N, ^{13}C′ and $^{13}C^{\alpha}$ are applied at 4.7, 118, 174 and 56 ppm, respectively. *Narrow* and *wide bars* indicate non-selective 90° and 180° pulses. The *single curved shapes* represent ^{13}C′-selective 180° sinc pulses of length $p^{\pi}_{C'} = 150$ µs, and the *triple curved shapes* ^{13}C ReBURP pulses (Geen and Freeman 1991) of length of $p^{\pi}_{C} = 500$ µs, respectively. *Vertical lines* connect centered pulses. ^{1}H-decoupling is achieved with WALTZ16 (Shaka et al. 1983) at a field strength γB_1 of 2.1 kHz and ^{15}N-decoupling with GARP (Shaka et al. 1985) at a field strength γB_1 of 1.25 kHz. The delays have the following values: $\tau_1 = 2.7$ ms, $\tau_2 = 16$ ms, $\tau_3 = 17$ ms, $\tau_4 = 60$ µs, $\Delta = 1/(2J_{HN}) = 5.4$ ms, and $T = \tau_{MQ} - 4p^{\pi/2}_{C'}/\pi$, where $p^{\pi/2}_{C'}$ is the length of the rectangular ^{13}C′ 90° pulse. The effective break in evolution of a scalar coupling to $^{13}C^{\alpha}$ during $p^{\pi}_{C'}$ is ≈50 µs and therefore is assumed to be of the same lengths as p^{π}_{N} or the inversion pulse train on $^{1}H^{N}$. Unless indicated otherwise, all radio-frequency pulses are applied with phase x. The phase cycle for the (ZQ-DQ) ACE subspectrum and the MMQ spectrum is: $\phi_1 = \{x, -x\}$; $\phi_2 = \{x\}$; $\phi_3 = \{x, x, x, x, -x, -x, -x, -x\}$; $\phi_4 = \{x, x, -x, -x\}$; $\phi_5 = \{-y\}$; $\phi_{rec} = \{x, -x, -x, x, -x, x, x, -x\}$. For the (ZQ + DQ) ACE subspectrum ϕ_3 and ϕ_4 are increased by 90°. The ACE ZQ and DQ spectra are obtained by addition and subtraction of the (ZQ − DQ) and (ZQ + DQ) ACE subspectra, respectively. Pulsed field gradients indicated on the line marked PFG are applied along the z-axis with duration/strength of: G_1, 1,200 µs/−9 G/cm; G_2, 2,000 µs/21 G/cm; G_3, 1,000 µs/15 G/cm; G_4, 200 µs/24 G/cm; G_5, 800 µs/6 G/cm; G_{N1}, 200 µs/18 G/cm; G_{N2}, 200 µs/−18 G/cm; G_6, 1,200 µs/−6 G/cm; G_7, 1,200 µs/18 G/cm; G_H, 40 µs/−18 G/cm; G_8, 400 µs/24 G/cm; G_9, 150 µs/15 G/cm. Quadrature detection in the ^{15}N(t_1) is achieved by the ECHO-ANTIECHO method (Kay et al. 1992) applied to ϕ_5 and gradients G_{N1} and G_{N2}, and in the MQ[^{13}C′,^{15}N](t_2) dimension by the States-TPPI method (Marion et al. 1989) applied to the phases ϕ_2, ϕ_4 and ϕ_{rec}

such pairs. One way to arrange these 6 pulses is proposed in reference (Carlomagno et al. 2000). Here, a different arrangement is chosen (Fig. 2). The minimal number of pulses on the relevant passively coupled spins is used, namely only one on $^{1}H^{N}$. Imperfections of pulses on the spins involved in the MQ coherences only lead to loss of signal due to the use of pulsed field gradients. In addition, $^{1}H^{N}$ is inverted by a 90° −202.5° −90° pulse train to further minimize the error.

All subspectra of the 3D ct-HNCO experiments were recorded with 36(t_1, N) × {ACE: 70/MMQ: 100}(t_2, MQ) × 512(t_3, H^{N}) complex points, $t_{1max} = 18.0$ ms, $t_{2max} = \{$ACE: 35.0/MMQ: 50.0$\}$ ms, $t_{3max} = 51.2$ ms, an interscan delay of 1.0 s and 8 scans per increment. The time domain data were multiplied with a square cosine function in the direct dimension and cosine functions in the indirect dimensions and zero-filled to 128 × 1024 × 2048 complex points. The mixing times τ_{mix} were 120 and 140 ms (ACE), and 70 and 100 ms (MMQ).

All experiments were performed on a BRUKER DRX600 MHz spectrometer, equipped with a z-axes gradient cryogenic probe, at 298 K. All spectra were processed and analyzed using the software package NMRPipe/NMRDraw/NlinLS (Delaglio et al. 1995). Peak heights were determined by parabolic interpolation.

Protein coordinates

A 1.1-Å high-resolution X-ray structure of GB3 is available (pdb code 1IGD, (Derrick and Wigley 1994)). In the present study, the positions of the H^{N} protons are of particular importance. Large sets of RDCs have been used to demonstrate out-of-plane H^{N} positions by refining the X-ray structure with the Xplor-NIH package (pdb code 2OED (Schwieters et al. 2003, 2006; Ulmer et al. 2003)). Subsequently, highly accurate RDCs have been used to orient H^{N}–N bond vectors and obtain associated order parameters with a direct interpretation which is independent of any restraining force fields (iterative DIDC method, (Yao et al. 2008a, b)). These H^{N}–N vectors have been superimposed on the backbone of 2OED to create a structure with highly accurate H^{N} positions (2OED-DIDC). This structure yields slightly better cross validation with $^{3}J_{HNH\alpha}$ scalar couplings and intraresidual and sequential $D_{HNH\alpha}$ RDCs than 2OED and significantly better ones than 1IGD (Vögeli et al. 2007, 2008). In addition, Clore and

Schwieters used RDCs, relaxation-derived H^N–N order parameters, and crystallographic B factors to generate twenty 8-member ensembles of structures (Clore and Schwieters 2006).

Results and discussion

Validation of measurements

Expansions of 2D planes cut from the ZQ, DQ and MMQ spectra together with slices along the MQ dimension are shown in Fig. 3. Extraction of the CCR rates in the ACE approach relies on a linear combination of relaxation rates of 8 individual components (see "Theory"). Equation 1 shows that potentially different scaling of peak intensities in the two subspectra is canceled out. Different scaling of the 4 components in one subspectrum due to additional relaxation pathways, pulse imperfections etc. are approximately also eliminated, because the MQ evolution is under minimal manipulation. The MMQ experiments suffer from the fact that the passively coupled spins are inverted by a H^N inversion pulse train and that the spins involved in the MQ coherences are 5 times inverted by nonselective 180° pulses on N and selective pulses on C′. On the other hand, this approach is more sensitive than ACE. If all peaks are assumed to be of approximately equal intensity the uncertainty of the CCR rate is by a factor $\approx \sqrt{2}$ smaller for MMQ than ACE. However, the more different the intensities are the larger the ratio of the errors because small intensities contribute over-proportionally. An additional error is introduced by the deviation from an ideal performance of the ^1H WALTZ decoupling schemes (Carlomagno and Griesinger 2000).

The CCR rates were measured twice with different mixing times with each approach to obtain a random error and identify potential systematic errors which are time dependent (ACE: 120, 140 ms; MMQ: 70, 100 ms). The random error of the averaged ACE data sets is 0.06 s^{-1}, whereas it is only 0.03 s^{-1} for the averaged MMQ data sets. These errors must be compared to a previously reported error obtained with a similar type of MMQ measurement on an ubiquitin sample of 0.16 s^{-1} (Carlomagno et al. 2000). The largest errors for ACE are obtained for residues 23, 26 and 54 exceeding 0.10 s^{-1} and additionally 6, 9, 33, 36, 37, and 40 exceeding 0.07 s^{-1}. No errors are available for residues 14, 38, 45 and 49. For MMQ, the largest errors are obtained for residues 21, 33, and 47 which are larger than 0.05 s^{-1} but none exceeds 0.07 s^{-1}. No errors are available for residues 19, 37 and 38. The CCR rates obtained from the ACE and MMQ approaches are compared in Fig. 4. An overall error can be obtained for the average of the two approaches. The half pairwise rmsd is 0.05 s^{-1}. The largest errors are obtained for residues 50 (0.11 s^{-1}) and 55 (0.09 s^{-1}). In addition, those of residues 45 and 56 are 0.08 s^{-1}, and those of 14, 23, 36, 41

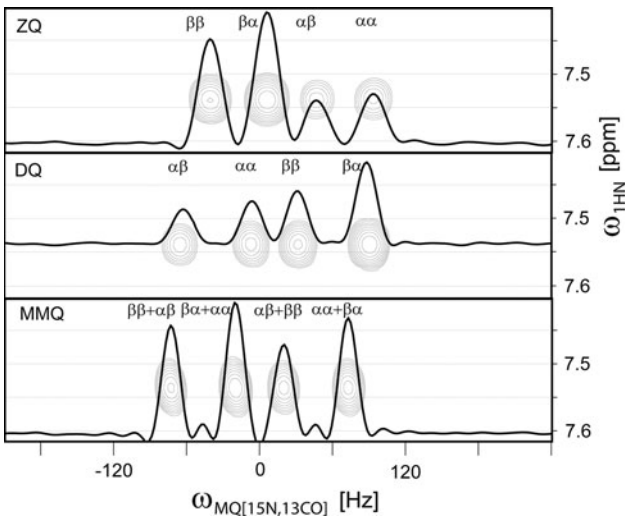

Fig. 3 2D MQ[^{15}N,$^{13}C'$]–$^1H^N$ planes and slices cut from the 3D ct-HNCO experiments showing the quadruplets of Leu12. The ZQ spectrum is shown on top, the DQ spectrum in the middle and the MMQ spectrum at the bottom. $\gamma\delta$ with γ, $\delta = \alpha$, β are the spin states with respect to N (γ) and C′ (δ). τ_{mix} was set to 120 ms and 100 ms for the ACE and MMQ experiments, respectively. The horizontal axes represent MQ frequencies in Hz units with arbitrary origins

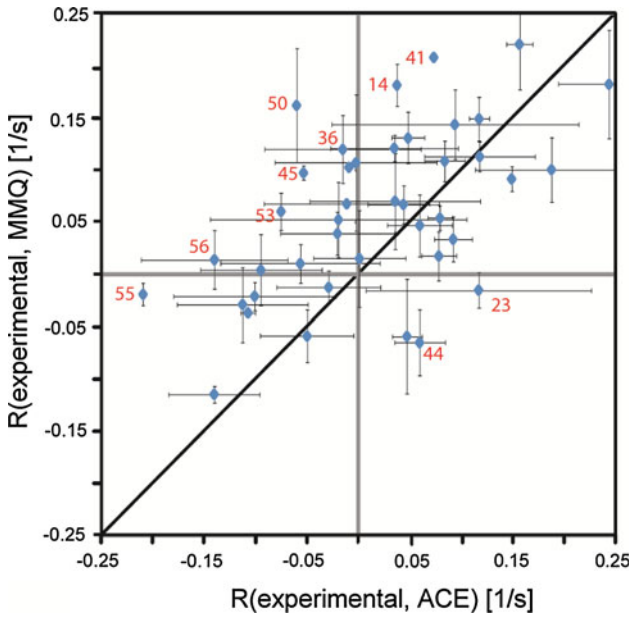

Fig. 4 Correlation plot of $R = R_{HNN/C\alpha C'} + R_{HNC'/C\alpha N}$ CCR rates obtained with the ACE and MMQ approaches. Error bars indicate random errors obtained individually for ACE and MMQ. The *black line* indicates a slope of 1. The most prominent outliers are marked with the corresponding residue numbers

Table 1 Statistics of C^{α}–C′–N and C′–N–H^N projection angles, and C^{α}–C′–N–H^N dihedral angles

Coordinates	C^{α}–C′–N projection angles[a] (°)	C′–N–H^N projection angles[a](°)	C^{α}–C′–N–H^N dihedral angles[a] (°)	ω (C^{α}–C′–N–C^{α}) dihedral angles[a] (°)	C^{α}–C′/N–H^N projection angles[a] (°)
1IGD[b]	116.2 ± 2.0	120.1 ± 1.0	−1.0 ± 3.0	179.0 ± 2.8	56.4 ± 1.9
2OED[c]	116.6 ± 1.6	119.5 ± 1.1	−1.2 ± 4.0	179.7 ± 5.0	56.2 ± 2.2
2OED-DIDC[d]	116.6 ± 1.6	119.3 ± 2.1	−1.1 ± 4.9	179.7 ± 5.0	56.0 ± 2.7
Ensemble, mean[e]	116.7 ± 1.5	119.2 ± 1.5	−0.4 ± 2.9	180.5 ± 4.2	55.9 ± 2.1

[a] Root-mean-square deviation of residue-specific averages from overall average

[b] X-ray structure from reference (Derrick and Wigley 1994)

[c] NMR structure from reference (Ulmer et al. 2003). Residue 41 is omitted

[d] H^N–N vectors derived from RDCs with the DIDC method and fitted to the 2OED backbone [see references (Ulmer et al. 2003) and (Yao et al. 2008a)]. Residue 41 is omitted

[e] Mean structure of the 160-conformer ensemble calculated in reference (Clore and Schwieters 2006)

and 53 are 0.07 s^{-1}. No errors are available for residues 15–22, 35, 46, 47 and 49. If the individual errors of the ACE and MMQ approaches are propagated the error is expected to be 0.03 s^{-1}. The larger error of the averaged ACE/MMQ values therefore indicates a residual systematic error of an additional 0.03 s^{-1}. It is possible that the majority of this error stems from the MMQ approach although it has a smaller random error than ACE as lined out in reference (Vögeli and Yao 2009). In order to avoid a possibly considerable impact of this systematic error both sets are compared to the structures individually as well as the average thereof. It should be noted that both approaches might produce some identical systematic errors since the two approaches are based on similar principles.

Validation of peptide plane geometry in high-resolution structures

The high-resolution structures feature small but relevant differences in the H^N–N/C′–C^{α} projection angles. These are primarily determined by the C^{α}–C′–N and C′–N–H^N projection angles, and weakly by the C^{α}–C′–N–H^N dihedral angles as demonstrated in Fig. 1 (see Table 1). While the averaged angles are very similar in all structures ($\approx$116.5° for C^{α}–C′–N; $\approx$119.5° for C′–N–H^N; $\approx$179.7° for ω; $\approx -0.9°$ for C^{α}–C′–N–H^N), the *per residue* variation is not as uniform. The ω angle has a root-mean-square deviation of 2.8° in 1IGD, but $\approx$5° in the NMR structures. Since the X-ray structure has protons placed in idealized positions, ω also determines the C^{α}–C′–N–H^N dihedral angle. On the other hand, NMR data is sensitive to the H^N nuclei and is likely to enforce the larger variation of the ω angle via the C^{α}–C′–N–H^N dihedral angle. The largest C^{α}–C′–N–H^N variation is observed in the 2OED structure with the independently derived H^N–N orientations from DIDC (2OED-DIDC, $\approx$5°), while the one of 2OED is somewhat smaller (4°) and the ensemble is similar to the X-ray structure ($\approx$3°). Note, however, that the CCR rates are weakly sensitive to the dihedral angle. The impact of explicit H^N placement is also observed for the C′–N–H^N projection angles with the largest variation for the 2OED-DIDC structure ($\approx$2°) being twice the one of the X-ray structure. A reversed effect is observed for the C^{α}–C′–N projection angles where the X-ray structure has the strongest variation ($\approx$2°) and those of all NMR structures are smaller ($\approx$1.5°). Here, NMR has no strong force field pulling the angle away from the default values. The projection angles between the main axes of the dipolar interactions (C^{α}–C′ and N–H^N) are with an average of 56.1° very close to the magic angle of 54.7°. The variation is largest for the 2OED-DIDC structure (2.7°), intermediate for 2OED and the ensemble (2.2° and 2.1°) and smallest for 1IGD (1.9°). All angles in the structures analyzed in this study are in close agreement with large surveys of X-ray structures deposited in the Cambridge Structural Database. The averaged C^{α}–C′–N angle is 116.9° with a standard deviation of 1.5° (Head-Gordon et al. 1991), ω is 179.6° with a standard deviation of 4.5° (MacArthur and Thornton 1996) and the C^{α}–C′–N–H^N dihedral angle −2.0° (MacArthur and Thornton 1996).

Interestingly, the correlation of the deviations from standard geometry between any pair of structures is poor (see Tables S1, S2 and S3 in the Supporting Information). Pearson's correlation coefficients for the C^{α}–C′–N projection angles are between 0.40 and 0.63, and between 0.14 and 0.47 for the C′–N–H^N projection angles. This results in values between 0.40 and 0.76 for the C^{α}–C′/N–H^N projection angles (see Table 2). In most cases slightly better correlation is observed for the predicted CCR rates (see Table 3). This effect is caused by the additional discrimination from anisotropic tumbling as CCR rates predicted assuming isotropic tumbling yields in most cases less

Table 2 Slope *s* (above diagonal, forced through the 0/0 coordinates) and Pearson's correlation coefficient *r* (below diagonal) of correlation plots of the C^{α}–C′/N–H projection angles

r/s *x* axis/*y* axis	1IGD[a]	2OED[b]	2OED-DIDC[c]	Ensemble, mean[d]
1IGD[a]	x	0.82	0.85	0.55
2OED[b]	0.76	x	0.68	0.60
2OED-DIDC[c]	0.62	0.57	x	0.31
Ensemble, mean[d]	0.51	0.64	0.40	x

[a] X-ray structure from reference (Derrick and Wigley 1994)

[b] NMR structure from reference (Ulmer et al. 2003)

[c] H^N-N vectors derived from RDCs with the DIDC method and fitted to the 2OED backbone [see references (Ulmer et al. 2003) and (Yao et al. 2008a)]. Residue 41 is omitted

[d] Mean structure of the 160-conformer ensemble calculated in reference (Clore and Schwieters 2006)

Table 3 Slope *s* (above diagonal, forced through the 0/0 coordinates) and Pearson's correlation coefficient *r* (below diagonal) of correlation plots of the CCR rates assuming anisotropic molecular tumbling

r/s *x* axis/*y* axis	1IGD[a]	2OED[b]	2OED-DIDC[c]	Ensemble, mean[d]
1IGD[a]	x	0.92	0.92	0.69
2OED[b]	0.79	x	0.85	0.73
2OED-DIDC[c]	0.69	0.66	x	0.53
Ensemble, mean[d]	0.53	0.72	0.33	x

[a] X-ray structure from reference (Derrick and Wigley 1994)

[b] NMR structure from reference (Ulmer et al. 2003)

[c] HN-N vectors derived from RDCs with the DIDC method and fitted to the 2OED backbone [see references (Ulmer et al. 2003) and (Yao et al. 2008a)]. Residue 41 is omitted

[d] Mean structure of the 160-conformer ensemble calculated in reference (Clore and Schwieters 2006)

agreement (see Table S4 in the Supporting Information). In conclusion, it is evident that true deviations from idealized geometry are not accurately represented in any of the high resolution structures analyzed here.

Fit to rigid structure

The experimental CCR rates are compared to those calculated from the 1.1-Å X-ray structure 1IGD (Derrick and Wigley 1994) and 2OED structure with RDC-optimized proton positions either calculated with the Xplor-NIH package (2OED) (Schwieters et al. 2003, 2006; Ulmer et al. 2003) or with the DIDC method (2OED-DIDC) (Yao et al. 2008a, b), and to the mean structure of the 160-member ensemble (Clore and Schwieters 2006). A correlation plot between averaged experimental ACE/MMQ and predicted CCR rates is shown in Fig. 5 and statistics listed in Table 4. Correlation plots for separate ACE and MMQ rates with error bars, and predicted on the basis of the various structures individually are presented in Figs. S1–S3 in the Supporting Information.

A complete list of rmsd values and Pearson's correlation coefficients obtained from correlation plots of predicted versus experimental CCR rates is shown in Table S6 in the Supporting Information. For all structures the correlation is substantially better with the MMQ than with the ACE data. This is not surprising given the lower random error of MMQ. In order to minimize possible systematic errors, correlations are also made with the average of the MMQ and ACE values. Rmsd values are comparable to those from MMQ alone. Remember that the experimental random errors are 0.06 s^{-1} and 0.03 s^{-1} for ACE and MMQ, respectively, and 0.05 s^{-1} for the averaged values (half pairwise rmsd). In the following the data is analyzed with the MMQ data set and the averaged MMQ/ACE data set.

The lowest rmsd values are in both cases obtained for 1IGD and the mean structure of the ensemble (between 0.61 s^{-1} and 0.69 s^{-1}). The largest rmsd is obtained for 2OED-DIDC with 0.93 s^{-1} and 0.96 s^{-1}. 2OED ranks in between. Surprisingly, vicinal *J* couplings defining the ϕ angle showed a reverse ranking with 2OED-DIDC having lower rms deviations in Karplus parametrizations and 1IGD the largest (Vögeli et al. 2007; Yao et al. 2008a, b). Apparently, the fitting of "free" H^N–N vectors is somewhat unphysical because no force field corrects for inconsistencies with the backbone heavy atoms. In addition, there is an uncertainty regarding the overall orientation of the vector set relative to the heavy-atom backbone. In Fig. 6

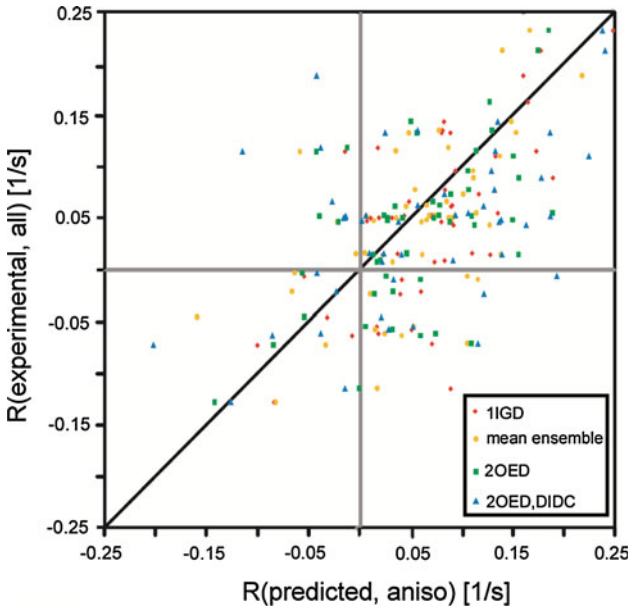

Fig. 5 Correlation plot of experimental $R = R_{HNN/C\alpha C'} + R_{HNC'/C\alpha N}$ CCR rates versus rates predicted from the 1IGD structure (Derrick and Wigley 1994) with proton positions calculated with the program MOLMOL (Koradi et al. 1996) (*red diamonds*), the mean structure of a 160-member ensemble (Clore and Schwieters 2006) (*yellow spheres*), the 2OED structure (Ulmer et al. 2003) (*green squares*), and 2OED with RDC-refined proton positions, 2OED-DIDC (Yao et al. 2008a, b). The experimental rates are obtained from averaged rates of the ACE and MMQ (all) approaches. The *black line* indicates a slope of 1

correlation plots between experimental and predicted rates are shown for 1IGD and the ensemble. Additional plots can be looked up in the Supporting Information.

The sole outlier for 1IGD with an error larger than 0.20 s^{-1} is residue 55. In addition, those with an error larger than 0.12 s^{-1} are residues 4 and 46. 55 is an extreme outlier for ACE (0.30 s^{-1}) but only a moderate one for MMQ (0.11 s^{-1}). Residue 4 is among the largest outliers for both ACE and MMQ. No value was obtained for 46 from ACE. Interestingly, MMQ produces no outlier with >0.15 s^{-1}.

Similarly for the mean ensemble, outliers with an error larger than 0.16 s^{-1} are residues 4 and 46. In addition, those with a larger error than 0.12 s^{-1} are residues 20, 53 and 55. Residues 4, 53 and 55 are extreme outliers for ACE (>0.20 s^{-1}) but only moderate ones for MMQ, while 20 and 46 have no value from ACE. MMQ produces no outlier with >0.17 s^{-1}.

Clearly, the impact of structural errors is much larger than the experimental errors. Interestingly, the two "best structures", 1IGD and the ensemble, produce the lowest correlation coefficient r between the CCR rates predicted from any pair of structures (Table 3). In order to obtain a "structural noise" an averaged structure is simulated by averaging their contributions. This hybrid structure has rms deviations of 0.060 s^{-1} (average ACE/MMQ) and 0.058 s^{-1} (MMQ) constituting the best structure. A lower limit for the structural error can be calculated by half the pairwise rmsd (0.03 s^{-1}). The propagated errors based on the experimental and structural errors are 0.06 s^{-1} (average ACE/MMQ) and 0.05 s^{-1} (MMQ). Thus, assumption of somewhat more than the lowest limit for the structural error would entirely explain the deviation of the predicted from the experimental CCR rates.

Table 4 Rmsd, Pearson's correlation r coefficient and slope s between experimental CCR rates and those predicted for a rigid molecule

Experimental data set	Coordinates	rmsd (Hz)[a]	s[a]	r[a]
Average MMQ/ACE	1IGD[b]	0.061[f]	0.73[f]	0.69[f]
	2OED[c]	0.072	0.64	0.61
	2OED-DIDC[d]	0.093	0.47	0.40
	Ensemble, mean[e]	0.068	0.70	0.59
	Average, ensemble, mean/1IGD	0.060	0.78	0.68
MMQ	1IGD[b]	0.062	0.82	0.65
	2OED-DIDC[d]	0.096	0.50	–
	Ensemble, mean[e]	0.069	0.80	0.52
	Average, ensemble, mean/1IGD	0.058	0.91	0.68

[a] $r_{HN} = 1.02$ Å and $r_{H\alpha C\alpha} = 1.09$ Å are assumed. X axis is the predicted and Y axis the experimental rate

[b] X-ray structure from reference (Derrick and Wigley 1994). Protons placed in idealized positions with the program MOLMOL (Koradi et al. 1996)

[c] Proton coordinates optimized with RDCs as carried out in reference (Ulmer et al. 2003)

[d] Proton coordinates optimized with RDCs obtained from 6 deuterated samples; rmsd values between predictions and experimental $^3J_{HNH\alpha}$ values of 0.32 Hz (Yao et al. 2008a, b). Residue 41 omitted

[e] Mean structure of the 160-conformer ensemble calculated in reference (Clore and Schwieters 2006)

[f] Residue 55 excluded

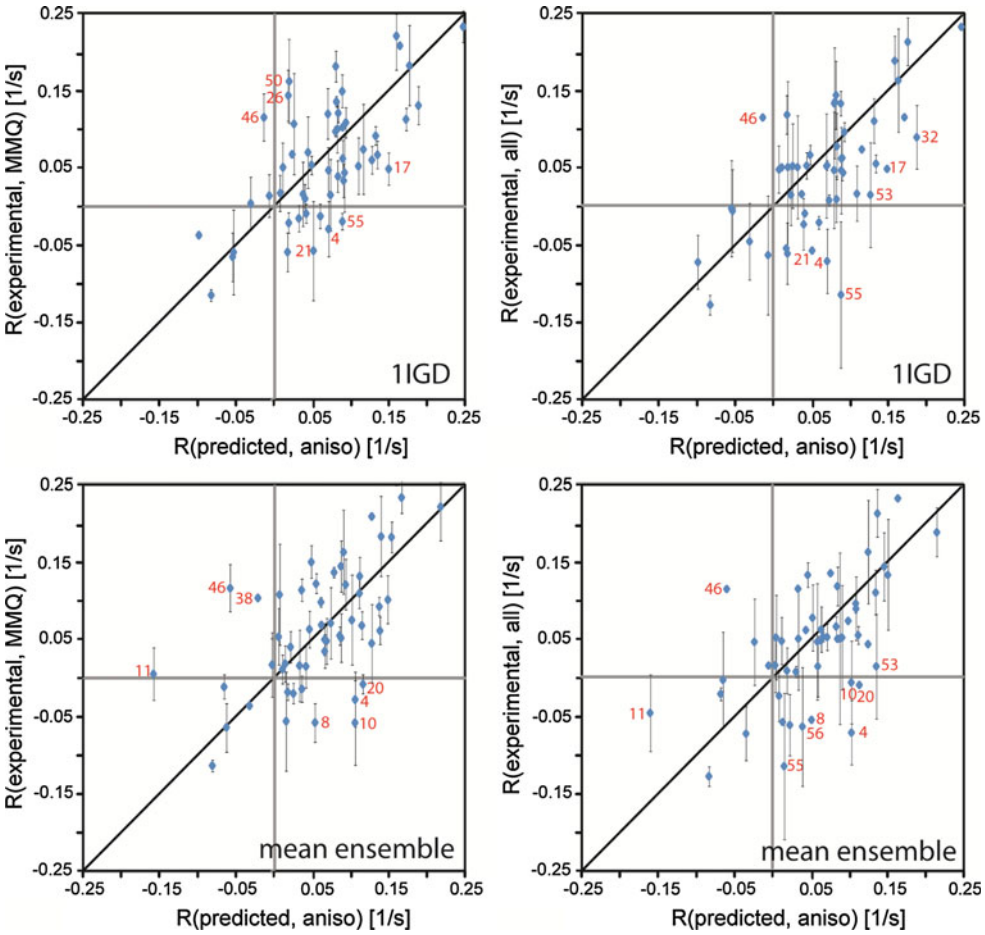

Fig. 6 Correlation plot of experimental $R = R_{HNN/C\alpha C'} + R_{HNC'/C\alpha N}$ CCR rates versus rates predicted from the 1IGD structure (Derrick and Wigley 1994) with proton positions calculated with the program MOLMOL (Koradi et al. 1996) (*top panels*) and the mean structure of a 160-member ensemble (Clore and Schwieters 2006) (*bottom panels*). The experimental rates are obtained with the MMQ approach (*left panels*), and averaged rates of the ACE and MMQ (all) approaches (*right panels*). Error bars for MMQ indicate random errors, and those for ACE/MMQ are obtained from the pairwise rmsd between ACE and MMQ. The *black lines* indicate a slope of 1. The most prominent outliers are marked with the corresponding residue numbers

Sequence specific analysis

It is instructive to analyze the CCR rates sequence specifically. Figure 7 shows the predicted and experimental CCR rates versus the amino acid sequence. The same trends can be observed for the experimental values obtained from the ACE and the MMQ approach (top panel). The largest absolute values are observed for the loops comprising residues 9–14, 20–22 and 38–41. The values are strictly positive and relatively large in the α helix. There is a clear alternating pattern of positive and negative values along the amino sequence in β strands 1, 3 and 4, whereas in strand 2 all values are positive in a decreasing manner. Large positive values have residues 4, 6, 8, 10, 40, 42, 44, 52, 55 and 56.

The bottom panel of Fig. 7 shows CCR rates predicted from the ensemble, 1IGD and 2OED-DIDC (Note that the predictions from the ensemble are based on averaging over the conformers rather than on the mean structure. Hence, the calculated rates do not represent a rigid structure. However, nearly identical values are obtained when predicted from the mean, vide infra). Generally, a similar spread of values is obtained as for the experimental values. This finding puts a stringent upper limit on the degree of geometry variation. The scatter is somewhat more pronounced in 2OED-DIDC than in the ensemble and 1IGD. In all the structures the α helix has similar trends as the β sheets. With the exception of strand 3, there is no alternating pattern in the β sheet for any of the structures. Not surprisingly, large differences in the rates of the various structures are obtained for the loops. Thus, these predicted rates are not reliable.

The deviations of the experimental from the predicted CCR rates are shown in Fig. S4 in the Supporting Information. Residues 4, 10, 46, 53 and 55 exhibit deviations larger than 0.1 s^{-1} for all structures (using the average of ACE/MMQ). In addition, there are several residues with deviations larger than 0.1 s^{-1} in 2OED-DIDC, namely residues 8, 12, 26, 29, 31, 36, 40, 41, 42 and 49. The other two structures have only three additional ones each: residues 17, 21, and 32 for 1IGD, and 11, 20, and 56 for the ensemble, respectively. Interestingly, residues 11, 20, and 46 are among the strongest outliers when RDCs $D_{HN(i)\text{-}H\alpha(i-1)}$ were compared to the ensemble (Vögeli et al. 2007). It is very likely that most single outliers are caused by insufficient individual structural representation. Obviously,

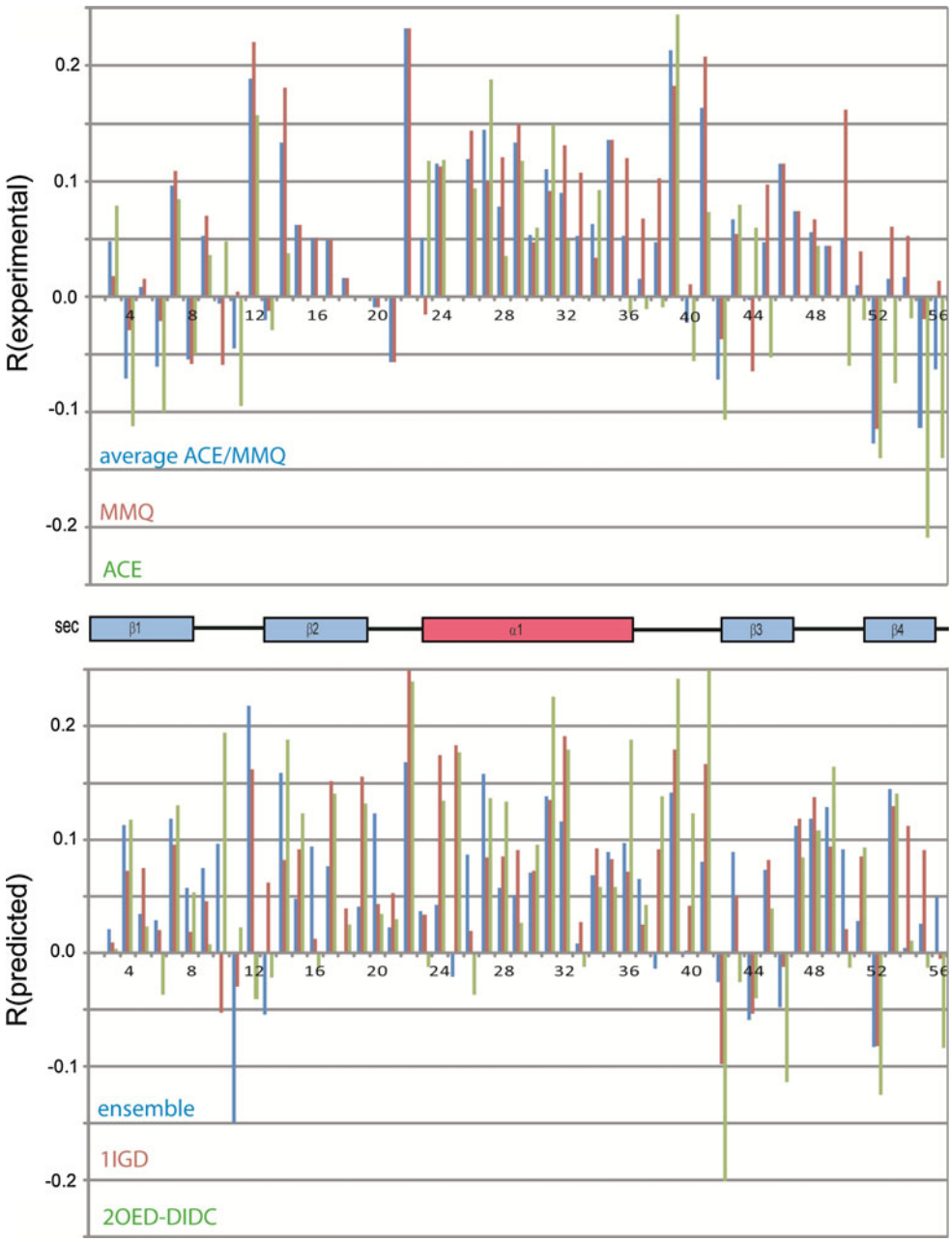

Fig. 7 $R = R_{d(HN)/d(COC\alpha)} + R_{d(NC\alpha)/d(HCO)}$ versus amino acid sequence. Top panel: Experimental values obtained with the averaged ACE/MMQ (*blue*), MMQ (purple), and ACE (*green*) approaches. Bottom panel: Values predicted on the basis of the ensemble (Clore and Schwieters 2006) (*blue*), X-ray structure 1IGD (Derrick and Wigley 1994) (purple), and 2OED with optimized protons 2OED-DIDC (Ulmer et al. 2003; Yao et al. 2008a, b) (*green*). The value expected for standard geometry and isotropic molecular tumbling is $+0.058\ s^{-1}$. Secondary structure elements are indicated between the panels

2OED-DIDC offers the worst representation. In all structures, many outliers are located in the loops that are generally not as well defined as other structural elements. Most other outliers are caused by the alternating pattern observed in the experimental rates.

Fit to dynamic structures

In the bottom panel of Fig. 7 the predicted CCR rates based on the ensemble representation (Clore and Schwieters 2006) are shown, and deviations from the experimental values are plotted in figure S4 in the Supporting Information. According statistics are listed in Table 5. The rms deviations between the predicted rates and those obtained from the average of ACE/MMQ is $0.069\ s^{-1}$, and from MMQ $0.070\ s^{-1}$, respectively. The outliers are the same as for the mean structure of the ensemble. The virtual identity indicates that the motion inherent in the ensemble has a minimal impact on the rates. Indeed, the correlation coefficient between rates obtained from the ensemble and its mean is 0.99 with a linear regression slope of 0.99.

An alternative way of incorporating motion into the rate prediction is provided by (4). Highly precise and accurate order parameters from RDCs are available for H^N–N and C'–C^α (Yao et al. 2008a, b). Rates predicted from 1IGD slightly improve the rmsd from the averaged ACE/MMQ

Table 5 Rmsd, Pearson's correlation r coefficient and slope s between experimental CCR rates and those predicted for a dynamic molecule

Experimental data set	Coordinates	rmsd (Hz)[a]	s[a]	r[a]
Average MMQ/ACE	1IGD, $S^{2,\ b,e}$	0.058[f]	0.83[f]	0.66[f]
	2OED-DIDC, $S^{2,\ c,e}$	0.083	0.54	0.41
	Ensemble[d]	0.069	0.69	0.58
	Ensemble, mean, $S^{2d\ e}$	0.068	0.81	0.53
	Average, ensemble, mean/1IGD, S^{2e}	0.060	0.90	0.64
MMQ	1IGD, $S^{2,\ b,e}$	0.062	0.93	0.61
	2OED-DIDC, $S^{2,\ c,e}$	0.087	0.58	–
	Ensemble[d]	0.070	0.79	0.51
	Average, ensemble, mean/1IGD, $S^{2,\ e}$	0.060	1.06	0.65

[a] $r_{HN} = 1.02$ Å and $r_{H\alpha C\alpha} = 1.09$ Å are assumed. X axis is the predicted and Y axis the experimental rate

[b] X-ray structure from reference (Derrick and Wigley 1994). Protons placed in idealized positions with the program MOLMOL (Koradi et al. 1996)

[c] Proton coordinates optimized with RDCs obtained from 6 deuterated samples; rmsd values between predictions and experimental $^3J_{HNH\alpha}$ values of 0.32 Hz (Yao et al. 2008a, b). Residue 41 omitted

[d] Mean structure of the 160-conformer ensemble calculated in reference (Clore and Schwieters 2006)

[e] RDC order parameters employed according to (4), uncorrelated motion assumed

[f] Residue 55 excluded

rates to 0.058 s^{-1} but do not change for MMQ. The correlation coefficient is even slightly lower. The slope of the linear regressions, however, increases from 0.73 and 0.82 to 0.83 and 0.93, respectively. Overall, an in-depth analysis cannot be pursued since the rmsd between the experimental and predicted rates is only slightly larger than their combined propagated error. In addition, the individual vector motions are not perfectly axially symmetric. For spin systems with bond projection angles close to the magic angle inequality 50 in reference (Vögeli 2010) is usually well fulfilled, and therefore (4) is not strictly valid. However, amplitude differences between in-plane and out-of-plane fluctuations are relatively small in regular secondary elements of GB3 (ca. 3°) (Yao et al. 2008b). In addition, if part of the fluctuations captured by the RDC order parameters occurs on the nanosecond timescale or is slower and correlated between A and B formula 4 underestimates the spectral density function and the true value is closer to the one obtained from the rigid-molecule approach (Vögeli 2010). Further error sources are the unknown order parameters of H^N–C^α and C′–N. Here, it is assumed that their product is identical to the one of the H^N–N and C′–C^α order parameters.

Interpretation of deviations

As shown above, the structural noise is at least 0.03 s^{-1}. There is additional uncertainty in the chosen bond lengths. In a recent publication the effective H^N–N bond length absorbing zero-point vibrations, but no angular fluctuations, has been determined to be 1.015 ± 0.006 Å (Yao et al. 2008b). Here, 1.02 Å is chosen. Ab initio calculation studies have reported on a C^α–C′ bond length variation of ca. ≈2% depending on the ϕ and ψ angles (Edison et al. 1994). In the present study, 1.525 Å was used (Engh and Huber 1991). C′ chemical shift calculations also suggested a strong pyramidalization of nitrogens in α helices (Sulzbach et al. 1995). Deviation of ≈15° from 180° for the ω angles are in agreement with experimental values (Sulzbach et al. 1995). For the structures analyzed in this study, no such trend is observed in the helices. According to Fig. 1, such a deviation would increase the predicted rates by 0.01 s^{-1}. Indeed, there is a weak accumulation of experimental rates that are larger than the predicted ones in the α helix (see Fig. S4 in the Supproting Information). The same effect, however, could also be obtained with adjustments of the projection angles. The authors also point out some limitations of their calculations such as the exclusion of solvation effects (Sulzbach et al. 1995).

The side chains of almost all residues with large positive rates in the β sheet are solvent exposed. A similar pattern has been observed in GB3 and ubiquitin for order parameters obtained from RDCs (Bouvignies et al. 2005; Lakomek et al. 2005). It was suggested that solvent-exposed side-chain motion is coupled with the pyramidalization of H^N–N groups (Lakomek et al. 2005). This would have a direct effect on the CCR rates under study. Interestingly, an unusual behaviour of β strand 2 has also been observed with H^N–N and H^α–C^α order parameters (Yao et al. 2008b). The former are lower and the latter less uniform than generally observed in the β sheet. It was speculated that this behaviour plays a role in molecular recognition.

An alternative explanation for the alternating patterns may be deduced from the fact that all β strands are involved in different structural formations to either side. The only parallel β sheet is formed between strands 1 and 4. The involved residues (with respect to the H^N atom) have negative values. Antiparallel β sheet is formed between strands 1 and 2, and strands 3 and 4. The corresponding residues in strand 1, 2 and 4 have positive values, while those in strand 4 have negative ones. The residues that are solvent-exposed in strands 2 and 3 have also positive values. Indeed, hydrogen bonds in antiparallel β sheets are nearly parallel to the involved H^N–N and C′=O bonds while they bridge the parallel sheet at an angle. Although not accounted for in the high-resolution structures these angles may be indicative of some distortion from ideal geometry. For solvent-exposed residues this distortion would not be expected as is indeed supported by corresponding positive values. The exceptionality of the negative values in strand 3 is then an indication that the rates cannot be solely explained by backbone secondary formation.

It cannot be entirely excluded that complex dynamic behaviour influences the rates to some observable extent. It is very likely that such motions would also affect the RDC order parameters. However, even for the most prominent case of the alternating pattern in β strand 1, no such pattern is observed for RDC order parameters. Thus, it is expected that such motions would affect all rates in regular secondary elements in a similar manner. Since rates obtained from loops are not interpreted the conclusions are not altered even if some complex dynamics is present.

Conclusion

New pulse sequences to measure CCR rates between H^N_i–N_i and C^{α}_{i-1}–C'_{i-1} dipoles are presented. Although these rates are very small they can be determined at very high precision and accuracy. The rates suggest clear deviation from idealized peptide plane geometry being thereby in fair agreement to high-resolution structures. However, the measured rates appear to allow a more accurate description of the plane geometry than the high resolution structures. For example, the rates show an alternating pattern in the β sheet with exception of strand 2, while the helix shows more positive values. This finding indicates that the backbone plane geometry does not only depend on the secondary structure but also on residue specific properties.

Acknowledgments Dr. Roland Riek is thanked for valuable discussions.

References

Bouvignies G, Bernado P, Meier S, Cho K, Grzesiek S, Bruschweiler R, Blackledge M (2005) Identification of slow correlated motions in proteins using residual dipolar and hydrogen-bond scalar couplings. Proc Natl Acad Sci USA 102:13885–13890

Bradley P, Misura KMS, Baker D (2005) Toward high-resolution de novo structure prediction for small proteins. Science 309: 1868–1871

Branden C, Tooze J (1999) Introduction to protein structure. Garland, New York

Bremi T, Brüschweiler R (1997) Locally anisotropic internal polypeptide backbone dynamics by NMR relaxation. J Am Chem Soc 119:6672–6673

Bremi T, Brüschweiler R, Ernst RR (1997) A protocol for the interpretation of side-chain dynamics based on NMR relaxation: application to phenylalanines of antamanide. J Am Chem Soc 119:4272–4284

Brunger AT (1993) XPLOR: a system for X-ray crystallography and NMR. Yale University Press, New Haven

Brutscher B, Skrynnikov NR, Bremi T, Brüschweiler R, Ernst RR (1998) Quantitative investigation of dipole-CSA cross-correlated relaxation by ZQ/DQ spectroscopy. J Magn Reson 130:346–351

Bytchenkoff D, Pelupessy P, Bodenhausen G (2005) Anisotropic local motions and location of amide protons in proteins. J Am Chem Soc 127:5180–5185

Carlomagno T, Griesinger C (2000) Errors in the measurement of cross-correlated relaxation rates and how to avoid them. J Magn Reson 144:280–287

Carlomagno T, Maurer M, Hennig M, Griesinger C (2000) Ubiquitin backbone motion studied via NH^N–$C'C^{\alpha}$ dipolar-dipolar and C'–$C'C^{\alpha}/NH^N$ CSA-dipolar cross-correlated relaxation. J Am Chem Soc 122:5105–5113

Carlomagno T, Bermel W, Griesinger C (2003) Measuring the χ^1 torsion angle in protein by CH–CH cross-correlated relaxation: a new resolution-optimised experiment. J Biomol NMR 27:151–157

Case DA (1999) Calculations of NMR dipolar coupling strengths in model peptides. J Biomol NMR 15:95–102

Chiarparin E, Pelupessy P, Ghose R, Bodenhausen G (1999) Relaxation of two-spin coherence due to cross-correlated fluctuations of dipole-dipole couplings and anisotropic shifts in NMR of N15, C13-labeled biomolecules. J Am Chem Soc 121:6876–6883

Clore GM, Schwieters CD (2006) Concordance of residual dipolar couplings, backbone order parameters and crystallographic B-factors for a small alpha/beta protein: a unified picture of high probability, fast atomic motions in proteins. J Mol Biol 355:879–886

Corey RB, Pauling L (1953) Fundamental dimensions of polypeptide chains. Proc R Soc Lond B 141:10–20

Daragan VA, Mayo KH (1997) Motional model analyses of protein and peptide dynamics using ^{13}C and ^{15}N NMR relaxation. Prog Nucl Magn Reson Spectrosc 31:63–105

Delaglio F, Grzesiek S, Vuister GW, Zhu G, Pfeifer J, Bax A (1995) NMRPipe: a multidimensional spectral processing system based on UNIX pipes. J Biomol NMR 6:277–293

Derrick JP, Wigley DB (1994) The third IgG-binding domain from streptococcal protein G. An analysis by X-ray crystallography of the structure alone and in a complex with Fab. J Mol Biol 243: 906–918

Deschamps M, Bodenhausen G (2001) Anisotropy of rotational diffusion, dipole-dipole cross-correlated NMR relaxation and angles between bond vectors in proteins. ChemPhysChem 2:539–543

Dunitz JD, Winkler FK (1975) Amide group deformation in medium rings lactams. Acta Cryst B31:251–263

Edison AS, Markley JL, Weinhold F (1994) Calculations of one-, two- and three-bond nuclear spin-spin couplings in a model peptide and correlations with experimental data. J Biomol NMR 4:519–542

Eisenberg D (2003) The discovery of the α-helix and β-sheet, the principal structural features of proteins. Proc Natl Acad Sci USA 100:11207–11210

Engh RA, Huber R (1991) Accurate bond and angle parameters for X-ray protein structure refinement. Acta Crystallog Sec A 47:392–400

Favro LD (1960) Theory of the rotational brownian motion of a free rigid body. Phys Rev 119:53–62

Fersht AR (1998) Structure and Mechanism in protein science. W.H. Freeman, New York

Früh D, Chiarparin E, Pelupessy P, Bodenhausen G (2002) Measurement of long-range cross-correlation rates using a combination of single- and multiple-quantum NMR spectroscopy in one experiment. J Am Chem Soc 124:4050–4057

Geen H, Freeman R (1991) Band-selective radiofrequency pulses. J Magn Reson 93:93–141

Goldman MJ (1984) Interference effects in the relaxation of a pair of unlike spin-1/2 nuclei. J Magn Reson 60:437–452

Gronenborn AM, Filpula DR, Essig NZ, Achari A, Whitlow M, Wingfield PT, Clore GM (1991) A novel, highly stable fold of the immunoglobulin binding domain of streptococcal protein G. Science 253:657–661

Güntert P, Mumenthaler C, Wüthrich K (1997) Torsion angle dynamics for NMR structure calculation with the new program DYANA. J Mol Biol 273:283–298

Hall JB, Fushman D (2003) Characterization of the overall and local dynamics of a protein with intermediate rotational anisotropy: differentiating between conformational exchange and anisotropic diffusion in the B3 domain of protein G. J Biomol NMR 27:261–275

Head-Gordon T, Head-Gordon M, Frisch MJ, Brooks CL, Pople JA (1991) Theoretical study of blocked glycine and alanine peptide analogues. J Am Chem Soc 113:5989–5997

Hu JS, Bax A (1996) Measurement of three-bond ^{13}C–^{13}C J couplings between carbonyl and carbonyl/carboxyl carbons in isotopically enriched proteins. J Am Chem Soc 118:8170–8171

Hu JS, Bax A (1997) Measurement of three-bond, $^{13}C'$–^{13}C beta J couplings in human ubiquitin by a triple resonance, E. COSY-type NMR technique. J Am Chem Soc 119:6360–6368

Kay LE, Keifer P, Saarinen T (1992) Pure absorption gradient enhanced heteronuclear single quantum correlation spectroscopy with improved sensitivity. J Am Chem Soc 114:10663–10665

Kloiber K, Schuler W, Konrat R (2002) Automated NMR determination of protein backbone dihedral angles from cross-correlated spin relaxation. J Biomol NMR 22:349–363

Koradi R, Billeter M, Wüthrich K (1996) MOLMOL: a program for display and analysis of macromolecular structures. J Mol Graphics 14:51–55

Kumar A, Grace CRR, Madhu PK (2000) Cross-correlations in NMR. Prog Nucl Magn Reson Spectrosc 37:191–319

Lakomek NA, Fares C, Becker S, Carlomagno T, Meiler J, Griesinger C (2005) Side-chain orientation and hydrogen-bonding imprint supra-τ_c motion on the protein backbone of ubiquitin. Angew Chem Int Ed 44:7776–7778

MacArthur MW, Thornton JM (1996) Deviations from planarity of the peptide bond in peptides and proteins. J Mol Biol 264: 1180–1195

Marion D, Ikura M, Tschudin R, Bax A (1989) Rapid recording of 2D NMR spectra without phase cycling: application to the study of hydrogen exchange in proteins. J Magn Reson 85:393–399

Meiler J, Prompers JJ, Peti W, Griesinger C, Brüschweiler R (2001) Model-free approach to the dynamic interpretation of residual dipolar couplings in globular proteins. J Am Chem Soc 123: 6098–6107

Pauling L, Corey RB (1951) The pleated sheet, a new layer configuration of polypeptide chains. Proc Natl Acad Sci USA 37:251–256

Pauling L, Corey RB, Branson HR (1951) The structure of proteins: two hydrogen-bonded helical configurations of the polypeptide chain. Proc Natl Acad Sci USA 37:205–211

Pelupessy P, Chiarparin E, Ghose R, Bodenhausen G (1999a) Efficient determination of angles subtended by C^{α}–H^{α} and N–H^{N} vectors in proteins via dipole-dipole cross-correlation. J Biomol NMR 13:375–380

Pelupessy P, Chiarparin E, Ghose R, Bodenhausen G (1999b) Simultaneous determination of Ψ and Φ angles in proteins from measurements of cross-correlated relaxation effects. J Biomol NMR 14:277–280

Pelupessy P, Ravindranathan S, Bodenhausen GJ (2003) Correlated motions of successive amide N–H bonds in proteins. J Biomol NMR 25:265–280

Perez C, Löhr F, Rüterjans H, Schmidt JM (2001) Self-consistent Karplus parametrization of ^{3}J couplings depending on the polypeptide side-chain torsion χ^{1}. J Am Chem Soc 123:7081–7093

Peti W, Meiler J, Brüschweiler R, Griesinger C (2002) Model-free analysis of protein backbone motion from residual dipolar couplings. J Am Chem Soc 124:5822–5833

Reif B, Hennig M, Griesinger C (1997) Direct measurement of angles between bond vectors in high-resolution NMR. Science 276: 1230–1233

Reif B, Diener A, Hennig M, Maurer M, Griesinger C (2000) Cross-correlated relaxation for the measurement of angles between tensorial interactions. J Magn Reson 143:45–68

Schwieters CD, Kuszewski JJ, Tjandra N, Clore GM (2003) The Xplor-NIH NMR molecular structure determination package. J Magn Reson 160:65–73

Schwieters CD, Kuszewski JJ, Clore GM (2006) Using XPLOR-NIH for NMR molecular structure determination. Prog Nucl Magn Reson Spectrosc 48:47–62

Shaka AJ, Keeler J, Frenkiel T, Freeman R (1983) An improved sequence for broad-band decoupling–WALTZ-16. J Magn Reson 52:335–338

Shaka AJ, Barker PB, Freeman R (1985) Computer-optimized decoupling scheme for wideband applications and low-level operations. J Magn Reson 64:547–552

Skrynnikov NR, Konrat R, Muhandiram DR, Kay LE (2000) Relative orientation of peptide planes in proteins is reflected in carbonyl-carbonyl chemical shift anisotropy cross-correlated spin relaxation. J Am Chem Soc 122:7059–7071

Sprangers R, Bottomley MJ, Linge JP, Schultz J, Nilges M, Sattler M (2000) Refinement of the protein backbone angle Ψ in NMR structure calculations. J Biomol NMR 16:47–58

Sulzbach HM, Schleyer PvR, Schaefer HF (1995) Influence of the nonplanarity of the amide moiety on computed chemical shifts in peptide analogs. Is the amide nitrogen pyramidal? J Am Chem Soc 117:2632–2637

Takahashi H, Shimada I (2007) Pairwise NMR experiments for the determination of protein backbone dihedral angle Φ based on cross-correlated spin relaxation. J Biomol NMR 37: 179–185

Tjandra N, Bax A (1997) Direct measurement of distances and angles in biomolecules by NMR in a dilute liquid crystalline medium. Science 278:1111–1114

Tolman JR (2002) A novel approach to the retrieval of structural and dynamic information from residual dipolar couplings using several oriented media in biomolecular NMR spectroscopy. J Am Chem Soc 12:12020–12030

Tolman JR, Al-Hashimi HM, Kay LE, Prestegard JH (2001) Structural and dynamic analysis of residual dipolar coupling data for proteins. J Am Chem Soc 123:1416–1424

Ulmer TS, Ramirez BE, Delaglio F, Bax A (2003) Evaluation of backbone proton positions and dynamics in a small protein by liquid crystal NMR spectroscopy. J Am Chem Soc 125:9179–9191

Vögeli B (2010) Comprehensive description of NMR cross-correlated relaxation under anisotropic molecular tumbling and correlated local dynamics on all time scales. J Chem Phys 133: 014501-1-13

Vögeli B, Pervushin K (2002) TROSY experiment for refinement of backbone Ψ and Φ by simultaneous measurements of cross-correlated relaxation rates and 3, 4JHαHN coupling constants. J Biomol NMR 24:291–300

Vögeli B, Riek R (2010) Side chain-backbone projections in aromatic and ASX residues from NMR cross-correlated relaxation. J Biomol NMR 46:135–147

Vögeli B, Yao LS (2009) Correlated dynamics between protein HN and HC bonds observed by NMR cross relaxation. J Am Chem Soc 131:3668–3678

Vögeli B, Ying JF, Grishaev A, Bax A (2007) Limits on variations in protein backbone dynamics from precise measurements of scalar couplings. J Am Chem Soc 129:9377–9385

Vögeli B, Yao LS, Bax A (2008) Protein backbone motions viewed by intraresidue and sequential H^N–H^α residual dipolar couplings. J Biomol NMR 41:17–28

Vugmeyster L, Pelupessy P, Vugmeister BE, Abergel D, Bodenhausen G (2004) Cross-correlated relaxation in NMR of macromolecules in the presence of fast and slow internal dynamics. CR Physique 5:377–386

Whitford D (2005) Proteins: structure and function. Wiley, Chichester

Winkler FK, Dunitz JD (1971) The non-planar amide group. J Mol Biol 59:169–182

Wüthrich K (1986) NMR od proteins and nucleic acids. Wiley, New York

Yang DW, Kay LE (1998) Determination of the protein backbone dihedral angle ψ from a combination of NMR-derived cross-correlation spin relaxation rates. J Am Chem Soc 120: 9880–9887

Yang DW, Konrat R, Kay LE (1997) A multidimensional NMR experiment for measurement of the protein dihedral angle Ψ based on cross-correlated relaxation between $^1H^\alpha$-$^{13}C^\alpha$ dipolar and $^{13}C'$ chemical shift anisotropy mechanisms. J Am Chem Soc 119:11938–11940

Yang DW, Gardner KH, Kay LE (1998) A sensitive pulse scheme for measuring the backbone dihedral angle Ψ based on cross-correlation between $^1H^\alpha$–$^{13}C^\alpha$ dipolar and $^{13}C'$ chemical shift anisotropy relaxation interactions J. Biomol. NMR 11:213–220

Yao L, Vögeli B, Torchia DA, Bax A (2008a) Simultaneous NMR study of protein structure and dynamics using conservative mutagenesis. J Phys Chem B 112:6045–6056

Yao LS, Vögeli B, Ying JF, Bax A (2008b) NMR determination of amide N–H equilibrium bond length from concerted dipolar coupling measurements. J Am Chem Soc 130:16518–16520